Low energy electron analysis and exfoliation techniques of transition metal dichalcogenides

Tambouli, Sharif El

Low energy electron analysis and exfoliation techniques of transition metal dichalcogenides

THESIS

submitted in partial fulfillment of the
requirements for the degree of

BACHELOR OF SCIENCE
in
PHYSICS

Author :	S.R.A. el Tambouli
Student ID :	s2029715
Supervisor :	Prof.Dr.Ir. S.J. Van der Molen
Second corrector :	Prof.Dr.Ir. T.H. Oosterkamp

Leiden, The Netherlands, July 5, 2023

Low energy electron analysis and exfoliation techniques of transition metal dichalcogenides

S.R.A. el Tambouli

Huygens-Kamerlingh Onnes Laboratory, Leiden University
P.O. Box 9500, 2300 RA Leiden, The Netherlands

July 5, 2023

Abstract

Transition metal dichalcogenides (TMDs, MX_2) are Van der Waals materials with properties such as the band structure depending on chemical structure and the number of layers. Low energy electron microscopy (LEEM) provides a manner of characterizing TMDs, by controlling the landing energies at which electrons reach the desired sample and measuring the reflection of the electrons. Besides real space imaging, our LEEM instrument is able to image reciprocal space, which is especially interesting to the characteristic hexagonal lattice of TMDs. This thesis will discuss a number of energy-resolution limiting factors. One of these factors is the energy distribution of electrons incident on the sample. It will discuss a method to correct for this energy dispersion and use it to decrease noise in electron reflectivity spectra. Also, fluctuations in electron current will be discussed and corrected for. Further, this thesis will examine oxidation of TMDs, as the rate of oxidation and impact on properties differs greatly depending on the specific composition of the TMD. It will discuss methods of exfoliating TMDs in vacuum, i.e. in situ, and show successful exfoliation in vacuum of around 10^{-6} mbar inside the LEEM. Also, the research will study exfoliation of Si/SiO_2 substrates with gold evaporated to produce large flakes of few-layer TMDs. This yielded MoS_2 few-layers flakes of up to 100 microns. The findings in this study regarding enhanced energy resolion in LEEM measurements of TMDs and improved techniques for TMD exfoliation will help the progress in understanding and characterization of TMD materials.

Contents

Chapter 1

Introduction

In recent years, there has been extensive research in 2D materials, or Van der Waals materials [1]. These materials are layered, existing from monolayers to bulk. Van der Waals materials are characterized by strong in-plane bonding and weak out-of-plane interactions. This feature enables exfoliation up to a single unit cell thickness [2].

Van der Waals material graphene has especially attracted a lot of attention [3]. Another group of materials has also been a prominent subject of research for some time: transition metal dichalcogenides (fig. 1.1) [1]. These transition metal dichalcogenides (TMDs) are a class of materials with the form MX_2, where M is a transition metal (for instance, Mo, W or Nb), and X is a chalcogen (S, Se or Te). In the TMD crystal, a transition metal atom is sandwiched between 2 chalcogen atoms [2].

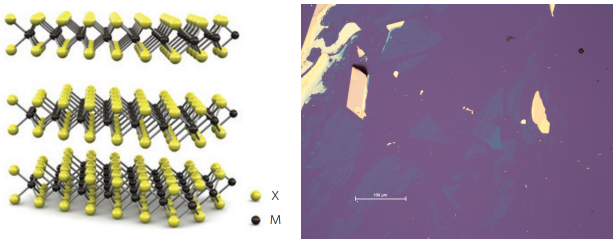

(a) (b)

Figure 1.1: ***(a)*** *Three-dimensional schematic representation of 3 layers of a TMD (MX_2), where M is transition metal atom (e.g. Mo, W or Nb), and X and chalcogen atom (S, Se or Te). Taken from [2]* ***(b)*** *Thin and thick flakes of MoS_2 on SiO_2-Au substrate*

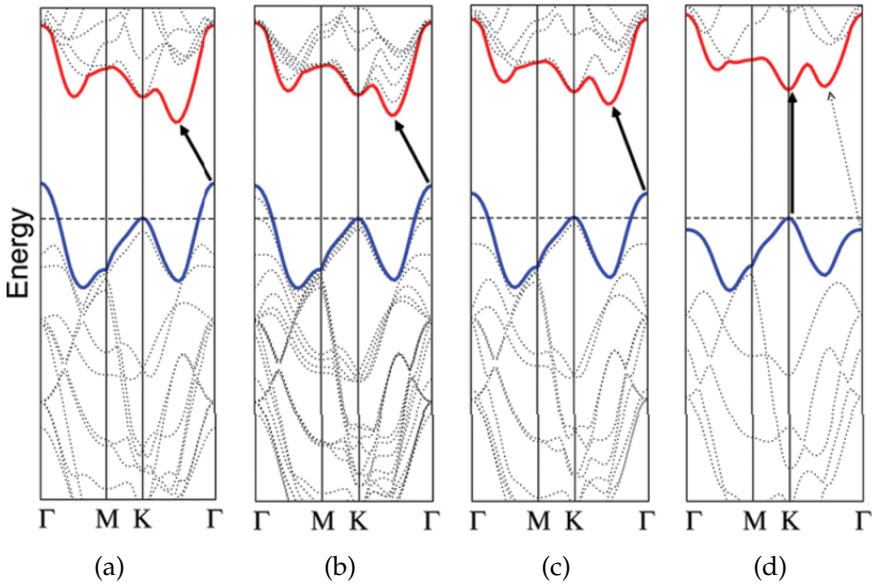

Figure 1.2: *Calculated band structure of MoS_2 in* ***(a)*** *bulk,* ***(b)*** *quadrilayer,* ***(c)*** *bilayer, and* ***(d)*** *monolayer. The arrows indicate the lowest energy transitions. Taken from [5]*

Due to their Van der Waals properties with weak interactions between layers, TMDs can relatively easily be exfoliated from bulk to a single layer. Interestingly, properties of the material may change, transitioning from bulk to few or single layer [4]. For example, the electronic band structure of TMDs changes when adding or removing layers from the material, shown in fig. 1.2.

To study TMDs, it is most interesting to chart the lowest energy states of materials in the region up to around 50 eV. In these energy states, the difference in band structure between TMDs is most visible. Also, changes in energy band structure due to the number of layers are visible at these lower energies. To measure at these energies, Low Energy Electron Microscopy (LEEM) can be used. In LEEM, the adsorption of electrons at the surface of materials can be studied with electron energy intervals down to 0.1 eV. Furthermore, due to the crystal lattice nature of TMDs, it would be interesting to study in diffraction space. To look at reflectivity in momentum space at low energies, a technique called angle-resolved reflected-electron spectroscopy (ARRES) can be exploited.

LEEM has the capability to map energy bands above the vacuum level.

With the right landing energy and the right angular momentum, corresponding to the energy state, an electron will be allowed to enter the material [6]. The LEEM setup is able to measure this, thus mapping the unique band structure for a TMD with a specific chemical orientation and the number of layers.

There are a few limiting factors to LEEM measurements. First of all, the electron beam used in LEEM is not monochromatic in kinetic energy but rather has a certain energy distribution. Second, the number of electrons released by the electron gun is not perfectly constant as well. These factors might lead to noise and inaccuracies in LEEM measurements. Another obstacle might be oxidation. Depending on the specific chemical composition, some TMDs are very prone to oxidation. This might change the electronic properties of the material, making it more difficult to map the properties of a sample.

The next chapter will go into more depth on the properties, similarities and differences of TMDs. Also, LEEM, the Leiden setup and ARRES will be discussed in detail. Further, it will discuss the implications of a non-monochromatic electron beam and inconstant electron current. Lastly, it will delve into oxidation of some materials and its consequences.

Chapter 2

Background

2.1 Transition Metal Dichalcogenides (TMDs)

Two-dimensional transition metal dichalcogenides (TMDs) is a group of materials in which the field of research is growing rapidly. Depending on the chemical composition, these materials might be categorized as (semi-)metallic, (semi-)conducting, insulating or even superconducting. TMDs all share the same composition (MX_2) of a transition metal layer (M) sandwiched between two chalcogen layers (X). Some of the most commonly used TMDs include molybdenum disulfide (MoS_2), molybdenum diselenide ($MoSe_2$) and tungsten diselenide (WSe_2) [7].

One of the main shared properties of TMDs is their hexagonally shaped crystal lattice due to their $X - M - X$ composition. This means, in reciprocal space, their first Brillouin zone will look like a hexagon with a characteristic threefold symmetry. This Brillouin zone contains high symmetry points Γ, K, K' and M (fig. 2.1). Although every TMD has a comparable hexagonal Brillouin zone, the lattice parameters differ, in both the in-plane and out-of-plane direction. The in-plane lattice parameters define the distance between Γ, K, K' and M, while the out-of-plane parameter defines the distance between separate layers, as well as the distance between transition metal atom and the chalcogen atom inside a layer [8].

Variations in chemical composition, as well as the number of layers, determine the energy band structure of a TMD [7]. For example, most semiconducting TMDs have a direct bandgap in monolayer, transitioning to an indirect band gap in bulk, with a few exceptions [10]. The band structures for MoS_2, $MoSe_2$, WS_2 and WSe_2 in monolayer, bilayer and bulk are

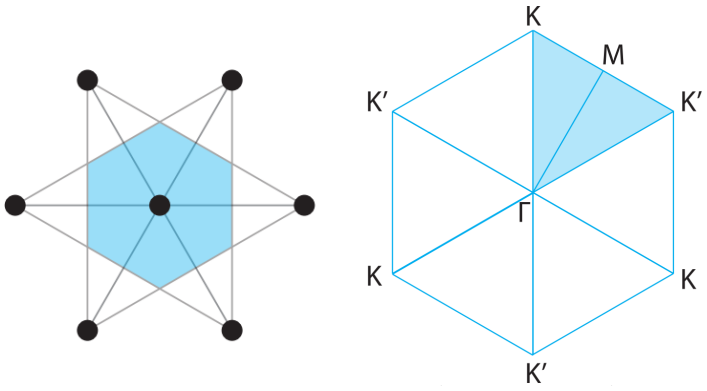

(a) (b)

Figure 2.1: ***(a)*** *Schematic representation of the diffraction pattern of a hexagonal lattice, occurring in TMDs. Black spots represent diffraction spots.* ***(b)*** *Hexagonal first Brillouin zone. Taken from [9]*

shown in fig. 2.2, simulated using DFT calculations, showing the change in band structure [11].

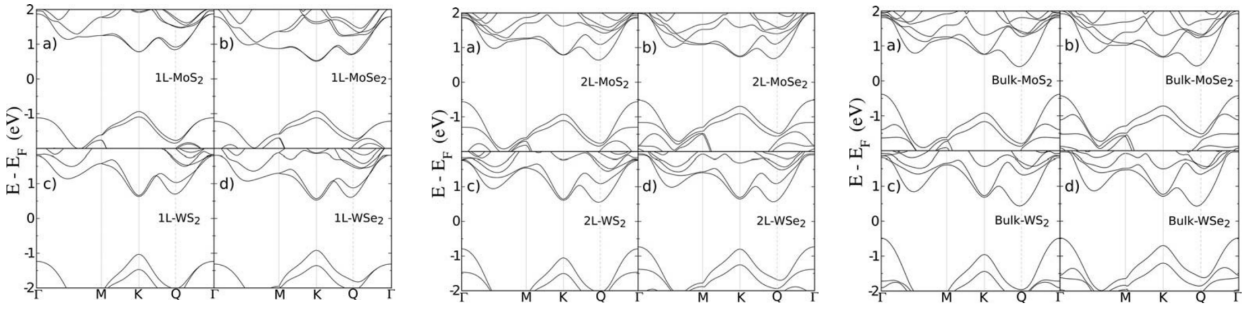

(a) (b) (c)

Figure 2.2: *Band structure of several TMDs, in* ***(a)*** *single layer,* ***(b)*** *bilayer and* ***(c)*** *bulk, demonstrating how the energy band structure is dependent on the number of layers. Taken from [11]*

There is also a characteristic interlayer energy state in TMDs which is absent in monolayers [12]. For example, in MoS_2 this state occurs around 5.4 eV. In a bilayer, this is present as a single state. Adding more layers, this state splits into two very similar states. Adding even more layers, the states continues splitting until the states are indistinguishable in bulk. [13].

This can be understood as resonance in electron wave functions. When an electron comes in contact with a layered material, it either passes through the layer or gets reflected. The electron that passes through can then either also pass through the next layer or get reflected. If this electron gets reflected, the wave functions of the electrons can interfere constructively, creating an extra energy state.

2.2 Oxidation

Another potential problematic factor for LEEM measurements of TMDs is oxidation. Scotch tape (or other kinds of tape) is still very widely used as a modus of exfoliation of TMDs [14]. While this is a very convenient method, exfoliation usually happens manually and immediately exposes freshly cleaved flakes to environmental gasses.

Experimentally, it is shown that monolayers of TMDs are especially prone to oxidation, the adsorption of O_2 [15]. While calculations show that perfect single-layer TMDs are not harmed by oxidation, O_2 can be chemically adsorbed onto a sample with single vacancies of chalcogen atoms in the crystal structure, which is the most common defect of TMDs. Some TMDs, such as MoS_2, are more prone to changes in electronic properties due to oxidation than others (especially $MoTe_2$ & WTe_2 are less affected) [15]. Also, the rate at which oxidation occurs might vary considerably between TMDs. For instance, $NbSe_2$ oxidizes at least 5 times quicker than MoS_2 [16]. This varying influence and rate of oxidation is reason to study exfoliation in (near) vacuum.

Chapter 3

Experimental setup

3.1 LEEM

Low energy electron microscopy (LEEM) is a surface probing technique in which electrons with very low energies interact with the surface of a sample, with a range of around 0-100 eV. A simplified overview of the Leiden LEEM setup is given in fig. 3.1. Here, the electron path is indicated in red, electron lenses in blue, apertures in green and deflectors in black [9].

The electrons exiting the gun have a initial energy of 15 keV. The beam is then rotated 90° in the prism towards the sample. The sample is however charged with a voltage of -15 kV + V_0. Thus the electrons are decelerated due to the negative charge. The user can manually set V_0 to vary the landing energy for the electron, from around -5 eV to +60 eV. For $V_0 < 0$, the surface charge will be too large for the electrons to reach the sample, and the electron will be fully reflected. This is called the *mirror mode*. For $V_0 > 0$, electrons will have just enough energy to reach the sample, with a landing energy equal to V_0. This allows for very low energy interactions, with a tweaking resolution of around 0.1 eV.

After reflection, the electrons are accelerated back to 15 keV, and the resulting image beam is magnified in an objective lens. The beam is then rotated 90° to its initial path. In the second prism, the beam is again rotated 90° towards an electron mirror. This mirror corrects for spherical and chromatic aberrations, which are induced by the field between the sample and the first objective lens. This aberration correction allows for a higher resolution compared to LEEM without the correcting electron mirror, ideally down to around 1 nm [17].

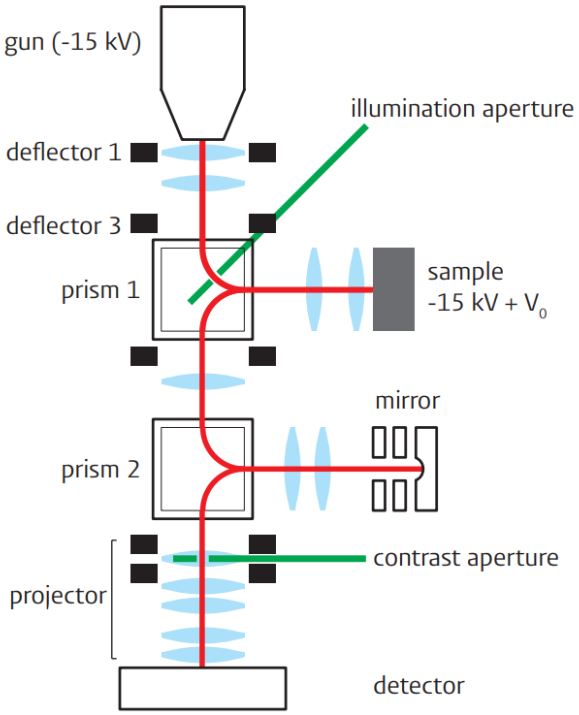

Figure 3.1: *Schematic overview of Leiden LEEM setup (ESCHER), used to study TMDs. Taken from [9]*

Finally, the beam is rotated again 90° back to its initial path. The electrons reach the detector, in which an image is formed [9]. This image is formed in a detector which counts the reflected electron.

The driving idea behind LEEM is that when reaching the surface of a sample, an electron can either get be reflected elastically from the surface, or enter the material, consequently not getting reflected. To link this to the band structure of TMDs, LEEM only maps energies above the vacuum level. If the landing energy and position in momentum space corresponds to an energy state, there is a higher probability of adsorption of electrons. Hence, a dip in reflectivity will occur at that energy and position. Reflectivity can then be plotted in an intensity-landing energy plot, called an IV curve. The band structure of samples differ depending on the material or the number of layers. Accordingly, different samples will give different IV curves [3].

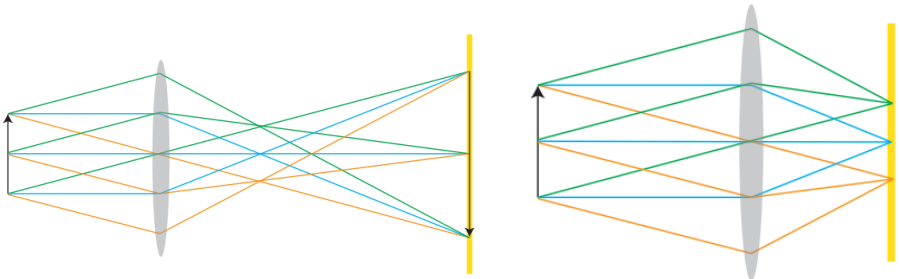

(a) (b)

Figure 3.2: *Simplified ray represtation of* ***(a)*** *real space plane* ***(b)*** *reciprocal space plane. Taken from [9]*

3.2 Diffraction space imaging & ARRES

The characteristic TMD crystal structure with threefold symmetry suggests that it is also interesting to observe TMDs in reciprocal space. The hexagonal lattice with $K - \Gamma - M$ high symmetry points is after all defined in momentum space. Further, the band structure of TMDs changes along these high symmetry lines. A theoretical plot of surface reflectivity of bulk MO_2 along these lines is shown in fig. 3.4.

A very useful feature of LEEM is that switching between imaging in real space and reciprocal space is possible. Imaging reciprocal space is referred to as Low Energy Electron Diffraction mode (LEED) [18]. Fig. 3.2 illustrates how both the real space image and reciprocal space image is constructed. The black arrow represents an object, or sample. The lines indicate the path of rays, with rays scattered at the same angle represented with the same colour. In real space, beams stemming from the same location are focussed in plane. This gives a regular (rotated) image with a certain magnification. Alternatively though, in reciprocal space, beams that are scattered at the same angle are projected on the detector. These beams thus have the same k-vector.

In LEEM imagining, it is possible to image the reciprocal. This is done by focusing in the reciprocal plane, as shown in fig. 3.2. To detect electrons with a certain k-vector, the electron beam is tilted to vary the angle of incidence, which is equal to the angle of reflection. This introduces an in-plane momentum $k_{parallel}$, as shown in fig. 3.3 [19]. This technique is called angle-resolved reflected-electron spectroscopy (ARRES). The tech-

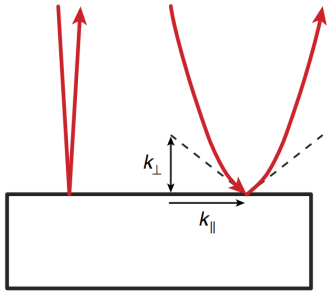

Figure 3.3: *Electrons reaching the sample at an angle will have an in-plane momentum $k_\parallel$. This is used to map the band structure of TMDs above vacuum level with ARRES. Taken from [19]*

nique can measure TMD lattices to reproduce plots such as fig. 3.4 experimentally [9].

3.3 Gun current fluctuations

Measurements with LEEM are based on electron count of the reflected electrons. The electron intensity is dependent on the reflectivity of the surface of the sample. This is the desired variable to measure. Unfortunately, the electron gun in the setup from which the electrons are initially emitted, is not perfect. The beam current is dependent on a number of external noise factors [21]. Because this noise directly affects the number of electrons emitted, this will consequently affect the number of electrons detected at the detector.

The LEEM setup can however measure gun current before the electrons hit the sample. This feature is possible in the illumination aperture in prism 1. Measuring this gives the possibility to reduce noise in IV curves.

3.4 Electron Energy dispersion

Ideally, the LEEM image in mirror mode ($V_0 < 0$) would produce a single spot in reciprocal space, indicating that all electron are reflected under the same angle. However, the diffraction spot, shown in fig. 3.5, seems to produce a line-like shape with asymmetric intensity decreasing in one direction. This is in fact caused by a kinetic energy distribution fo the

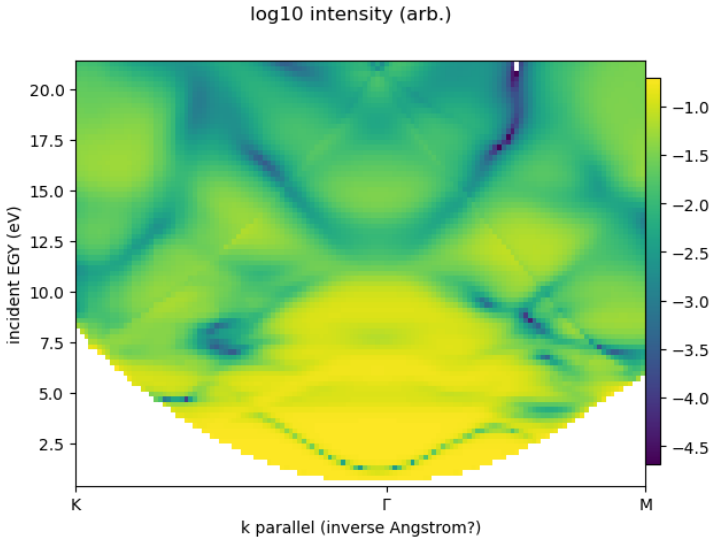

Figure 3.4: *Theoretical reflectivity of bulk MoS_2 hexagonal lattice along high symmetry lines $M - \Gamma - K$. Data used from [20]*

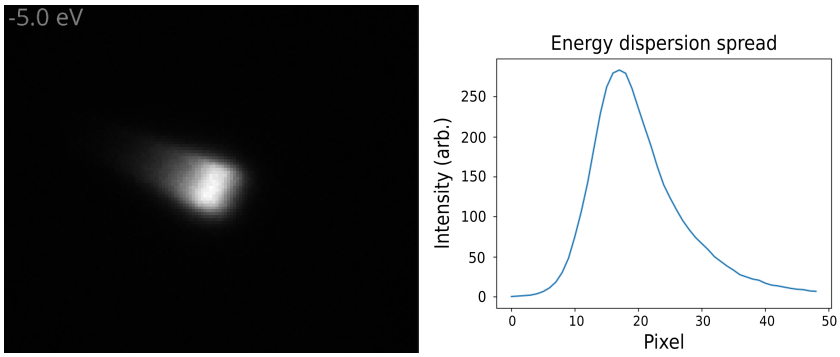

(a) (b)

Figure 3.5: ***(a)*** *Mirror mode ($E < 0$) with dispersion in one direction. This intensity loss is due to a distribution of kinetic energy in the incidence electron beam as a result of tunnelling effects at the time of generation* ***(b)*** *Intensity spread over a linecut of (a) in the direction of intensity loss*

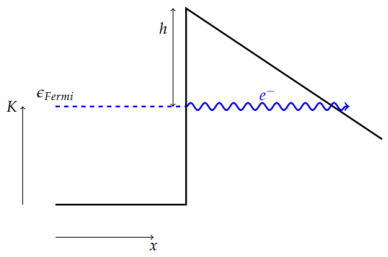

Figure 3.6: *Tunneling process of electrons extracted from electron gun tip visualized. The energy barrier tilts down when an extraction voltage is applied to the tip. This allows electrons with to tunnel through the barrier.*

electrons emitted from the electron gun.

This energy distribution in kinetic energy of individual electrons has been described by Fowler and Nordheim [22]. In an electron gun, electrons are emitted by applying a certain extraction voltage to the tip of the gun. This allows electrons with lower energies to tunnel out of the tip. This effect is visualised in fig. 3.6.The chance of tunneling out of the tip drops off exponentially with the energy, going to zero for energies lower than the Fermi energy. The electrons available for tunneling are described by the Fermi-Dirac distribution, and the full energy distribution is described by:

$$j(\epsilon) = z_S f_{FD} \frac{2F}{3b\phi^{1/2}} \exp\left(\frac{b\phi^{1/2}(\frac{3\epsilon}{2} - \phi)}{F}\right) \tag{3.1}$$

With z_s Sommerfeld's electron supply constant, f_{FD} the Fermi-Dirac distribution, F the field gradient depending on the extraction voltage, ϕ the work function for the tip and ϵ the energy of electron relative to the Fermi level. b is a constant defined by the electron mass m_e and charge e: $b = \frac{4\sqrt{2m_e}}{3e\hbar}$ [23].

In the LEEM setup, electrons are turned in the prisms a number of times due to a magnetic field, ideally 90°. The Lorentz force law for a moving electron states, assuming $\vec{E} = 0$:

$$\vec{F} = q_e(\vec{v_e} \times \vec{B}) \tag{3.2}$$

Here, $\vec{F}$ is the force vector on the electron, q_e the electron charge, $\vec{v_e}$ the velocity of an electron and $\vec{B}$ the applied magnetic field. The magnetic field is set perpendicular to the electron velocity, hence $\vec{v_e} \times \vec{B} = v_e B$. Setting

the resulting Lorentz force equal to the centripetal force, and rearranging the terms, this results in:

$$r_g = \frac{mv_e}{qB} \tag{3.3}$$

With r_g the gyroradius, i.e. the radius of the motion of the electron in a magnetic field. The velocity of the electron is only dependent on the applied (electric) potential.

$$v_e = \sqrt{\frac{2\epsilon_e}{m_e}} \tag{3.4}$$

With m_e the electron mass. The kinetic energy distribution described by Fowler and Nordheim leads to a slight variation in the gyroradius r_g. This results in slight deviations from the 90° turns in the several prism passes, producing an elongated spot in diffraction space, as shown in fig. 3.5.

This feature of the LEEM adds noise and inaccuracies to measurements. However, if this spread is defined and quantified, this can be filtered out and could even improve measurements.

3.5 Exfoliation

Transition metal dichalcogenides are, as explained in the previous chapters, a group of Van der Waals metarials. These type of materials are characterized by strong in-plane bondings, but weak interactions between layers. Some properties of TMDs change, transitioning from bulk crystals to few or single layers. Consequently, thin flakes of TMDs is an interesting subject of research. Monolayers of TMDs typically have a thickness of 0.6-0.7 nm [24].

Due to this weak out-of-plane van der Waals force interaction in TMDs, exfoliating thinner flakes is relatively easy. This is done by pressing a crystal of the desired TMD onto a piece of scotch tape, leaving a thick layered crystal of the TMD on the tape. Fig. 3.7 shows a very thick flake of MoS_2. This tape is then folded onto itself slightly misaligned two or three times to create thinner flakes. The resulting tape with flakes is called the *mother tape*. Next, another piece of scotch tape is pressed onto a desired patch of flakes from the mother tape, preferably with some large intact flakes. This

Figure 3.7: *MoS_2 crystal on scotch tape. This tape could serve as a mother tape for the exfoliation process of MoS_2.*

is again folded onto itself a number of times to further exfoliate layers. The resulting tape is the *generation I* tape. The goal is to obtain flakes as thin as possible and as intact as possible. Depending on visual judgement of the flakes, a number of generations can be made. When the flakes are sufficiently thin, the tape is pressed onto the desired substrate to exfoliate flakes one last time, leaving thin flakes on the substrate.

This exfoliation method usually happens manually in atmospheric pressure. In the previous chapter, the potentially high influence of oxidation in TMDs is discussed. To prevent this oxidation, it is desirable to perform the exfoliation *in situ*, i.e. in a vacuum. However, regular tape is usually avoided in vacuums due to their high outgassing potential. Mainly the diffusion of H_2O from the tape can be a source of contamination of the vacuum [25]. Therefore, Kapton tape will be used for the process. Kapton tape is regularly used in (ultra-)high vacuums on account of its property to maintain its structure and adhesiveness in low-pressure environments [26].

While a glove box with inert gas, such as nitrogen, does provide a practical and versatile environment to exfoliate, the transfer to the LEEM, in which the sample is measured, yields some time period for the flakes to exfoliate. To work around this transfer, the exfoliation will happen inside the LEEM. The most practical location would be in the loadlock, with a pressure of the order of 10^{-6} mbar, where you have manual control over the transfer arm, which can move and twist along the direction of the arm.

Oxidation mainly happens at the surface layers of a TMD, with the underlying layers almost unaffected by oxidation [27]. Thus, it would suffice

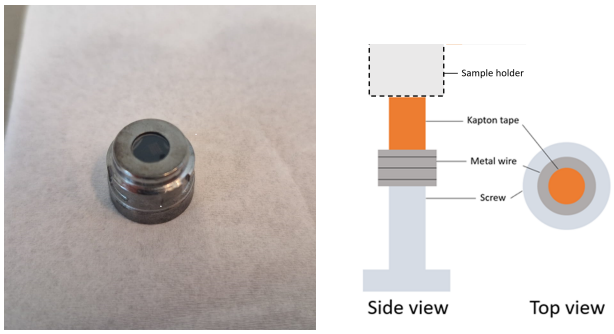

(a) (b)

Figure 3.8: (a) *Leiden LEEM sample holder with substrate.* ***(b)*** *Design for in situ exfoliation instrument. Kapton tape is stretched over the flat tip of the screw. The tip is pushed onto the revealing part of the substrate, with TMD flakes between the substrate and the Kapton tape. After placing the sample holder with the screw adhered inside the vacuum, the screw is removed to exfoliate flakes in situ.*

to remove to remove the top (few) layers in situ. There are two options for this in situ exfoliation. Firstly, it is possible to perform the full exfoliation as described before. The initial flake will be touched down on the substrate outside a vacuum. Then, the top layers of the flakes on the sample will be exfoliated inside the loadlock. This technique would consequently leave unoxidized flakes of the TMD. A potential obstacle is that it is uncertain which flakes will get adhered to the tape, and thus exfoliated. Another option is to collect flakes on Kapton tape after creating flakes ex situ by pressing it down on the final generation scotch tape. The tape will then be applied the tape to the substrate and removed *after* putting the substrate with tape inside a vacuum. Assuming no flakes will get completely detached from the adhesive tape, every flake on the substrate will be unaffected by oxidation.

There are some practical difficulties with in situ exfoliation. The sample holder, shown in fig. 3.8(a), has a round aperture of 5 mm in diameter, with only this area of the substrate revealed. To cover as much substrate as possible with the (Kapton) tape but also prevent contamination of the sample holder, the in situ exfoliation would ideally happen with a piece of tape with a surface area of the same size as the aperture. A design for an in situ exfoliation instrument in fig. 3.8(b). Here, a piece of Kapton tape is "stretched" over the tip of the screw and fixed using metal wire. The head of the screw could be used to knock or pull the stamp off of the substrate.

Chapter 4

Results & discussion

4.1 Noise reduction

This section will delve into some noise factors and how to reduce these factors. First, it will discuss the energy dispersion, as described in section 3.4, and how to reduce this. Next, it will consider reducing noise by weighing the average to reduce fluctuations. Finally, correcting for fluctuations in gun current, i.e. fluctuations in the number of electrons emitted by the electron gun is discussed.

4.1.1 Energy dispersion correction

As discussed in the previous chapter, noise of LEEM measurements could be reduced by using the energy dispersion property of the electron gun. An IV curve is calculated using the intensity of pixels in frames, where each frame corresponds to an certain energy. Averaging over multiple pixels is a good way to reduce noise affecting individual pixels. This can be done by taking a linecut along the direction of intensity loss, as shown in fig. 4.1. If $I_n(E)$ is the function that describes the intensity of pixel n at energy E, the intensity at a specific energy can then be calculated:

$$I_{average}(E) = \frac{1}{N} \sum_{n=1}^{N} I_n(E) \tag{4.1}$$

With $I_{average}(E)$, the calculated intensity curve, I_n the intensity curve at the nth pixel, and N as the number of pixels in the linecut. But, as is explained in the previous chapter, due to the energy dispersion of the electron, pixels in a frame do not represent electrons with exactly the same

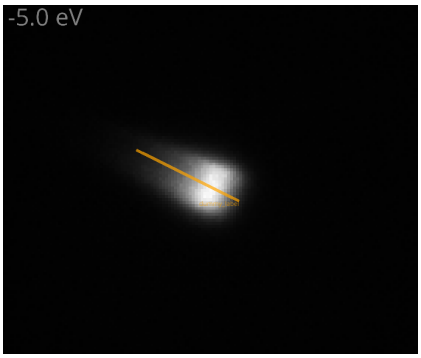

Figure 4.1: *Linecut through diffraction spot. By measuring long the linecut the intensity of pixels at frames with a range of electron landing energies, an IV curve can be constructed.*

energy. Due to a distribution in kinetic energy, the electrons will land on the sample at a slightly different angle, which is in a diffraction space measurement represented as a different position on the detector. A more correct averaging method can take this dispersion into account while also reducing frame-specific noise factors:

$$I_{corrected,average}(E) = \frac{1}{N}\sum_{n=1}^{N} I_n(E - \delta n) \tag{4.2}$$

With δ the energy per pixel.

To determine the value of δ, one can use some characteristic intensity feature of a sample. For a TMD, the first intensity dip can be used. Without any energy dispersion, this dip in intensity would appear uniformly over the spot. Due to the energy dispersion, this is not the case. The dip 'shifts' along the diffraction spot in a certain direction, as shown in fig. 4.2(a)-(b).

One can assume this dip occurs at exactly the same true landing energy of the electron. Then, the energy per pixel can be calculated:

$$\delta = \frac{\Delta E}{\Delta pixel_{minimum}} \tag{4.3}$$

From multiple LEEM measurements, this energy per pixel is determined at $\delta = 2.275 \cdot 10^{-2} \pm 2.4 \cdot 10^{-6}$ eV per pixel.

With this value, it is also possible to check the full width at half maximum for the electron gun. This calculation is done in appendix A.

(a) (b) (c)

Figure 4.2: ***(a), (b)*** *Diffraction spots of MoS_2 at different energies (as indicated). The characteristic first dip in electron reflectivity can be observed as a moving dip in intensity at these energies.* ***(c)*** *Found minima of intensity of frames shown in (a) & (b), along the shown linecuts. Using the difference in energies of the frames and the difference in position of minima, the energy per pixel is calculated.*

Ideally, $I_n(E)$ is a continuous function, which would make averaging over all $I_n(E)$ after shifting δn perfectly possible. Because of the nature of LEEM measurements however, with discrete energy steps, the resulting intensity is not continuous. This makes averaging over measured intensity values a bit less straightforward. Here, the choice is made to round the shift δn to the nearest energy step. For example, if the measurement step ΔE is equal to 0.1eV, for $\delta n < 0.05$, the intensity will not be shifted. For $0.05 < \delta n < 0.15$, the intensity will be shifted by 0.1eV, and so on.

4.1.2 Weighing base intensity

Another factor that induces noise into measurements by taking the regular average, is the fact that different measuring positions have a different 'base' intensity. While characteristic features of intensity are exhibited at every position, the exact value of the intensity differs greatly, especially along the axis of energy loss discussed in the previous section. The values of $|I_n(E) - I_{average}(E)|$ are consequently higher. Hence the variance of the average is higher, resulting in more noise in the average IV curve.

Because the values of the measured intensity are not normalized, it is allowed to multiply the intensity values at a certain pixel with a constant factor A for every landing energy, without changing the measure-

Version of July 5, 2023– Created July 5, 2023 - 14:16

ment. The IV curves for every pixel can be multiplied with some specific normalization factor to overlay the curves, to bring the variance of the average down. While the choice for the normalization factor is somewhat arbitrary, a logical choice would be to normalize with respect to the pixel with the highest intensity. In mirror mode, i.e. $E < 0$, every electron is reflected, so a constant intensity is expected. The average intensity serves as a good reference point. The normalization constant can be calculated:

$$A_n = \frac{\sum I_{maxpixel}(E < 0)}{\sum I_n(E < 0)} \tag{4.4}$$

Hence, the resulting corrected intensity is:

$$I_{n,corrected}(E) = A_n I_n(E) \tag{4.5}$$

Fig. 4.3(a) shows an IV curve as a result of taking the regular average. Fig. 4.3(b) shows the resulting IV curve if the pixel intensity is corrected for energy dispersion and normalized. Visually, the improved IV curve looks smoother than the regular average.

Fig. 4.3(b) and (d) show the absolute first difference for the IV curves, so for energy E, with energy steps ΔE:

$$|\Delta I(E)| = |I(E + \Delta E) - I(E)| \tag{4.6}$$

These differences are taken after normalizing the curves. For a perfectly smooth curve, one would expect also perfectly smooth first differences. If the first differences are more erratic, more noise is in the signal, in this case the IV curve. We are interested in the absolute value of the first differences to see whether this value follows a smooth course.

In the first differences, fig. 4.3(b) is a lot more erratic than (d), which is following a clearer trend. This suggests that the IV curve in fig. 4.3(c) is indeed more smooth, after the correction for energy dispersion and weighing the average. Further, around $E = 0$, i.e. the transition from mirror mode to the first characteristic dip, the first difference has a high but smooth peak for the correct IV curve. This is due to the increased slope of the IV curve approaching the first dip. Because these features occur over a small energy interval, not correcting for energy dispersion will lead to some convolution of the signal and energy distribution of the electron gun, which broadens the dip. This effect is removed in the improved method, thus resulting in a energy resolution better than the gun spread.

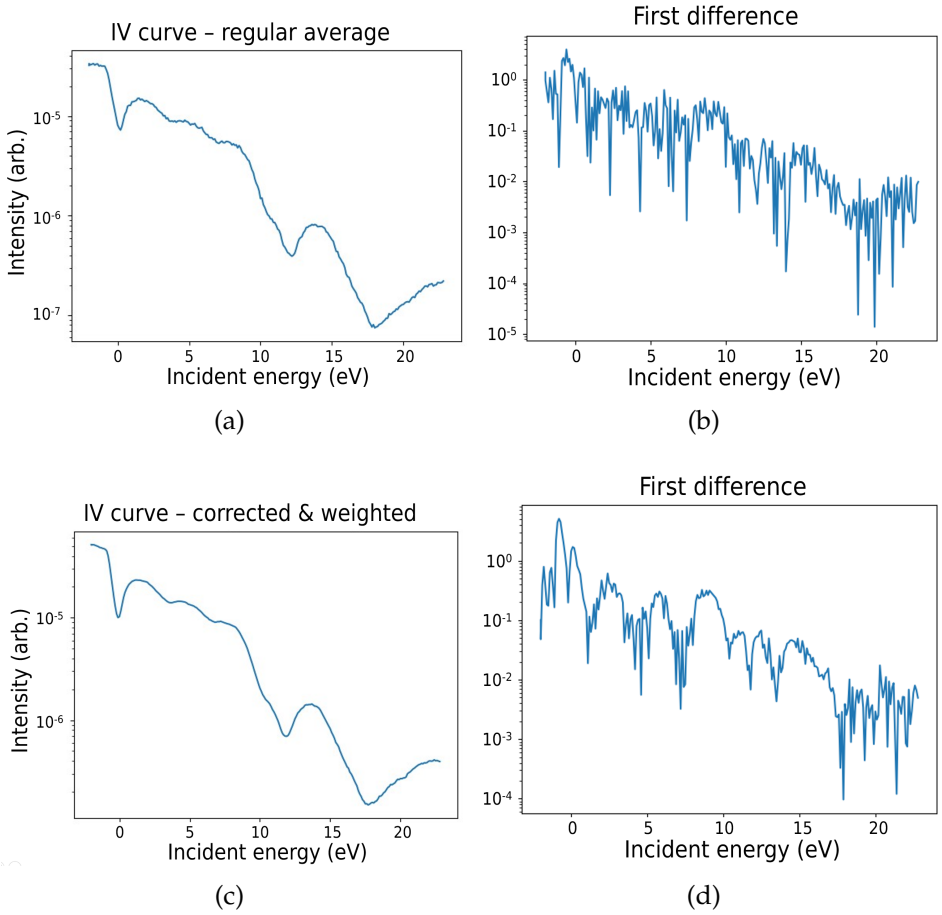

Figure 4.3: ***(a)*** *IV curve of MoS_2, calculated with the regular average over a line-cut.* ***(b)*** *First difference of IV curve shown in (a)* ***(c)*** *Improved IV curve, corrected for energy dispersion & normalized before averaging* ***(d)*** *First difference of IV curve shown in (a). Visually, the IV curve shown in (c) is smoother. This is confirmed by the first difference shown in (b) & (d). For a smooth curve, one would expect the first difference ($I(E + \Delta E) - I(E)$) to also follow a smooth curve, as there are no sudden changes in value expected. The first differences of the uncorrected curve are significantly more erratic than the first differences of the corrected curve, showing an improvement of the IV curve.*

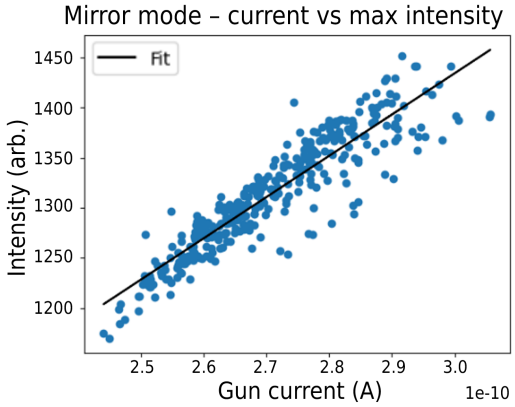

Figure 4.4: *The measured gun current of mirror mode ($E < 0$) frames and the resulting measured intensity. The gun current, the number of electrons emitted by the gun, is not constant. This plot shows a positive linear relation between the measured gun current (before hitting the sample) and the measured intensity in the detector. The black line is a linear fit. This relation can be used to correct for fluctuations in gun current for every E.*

4.1.3 Gun current correction

Another factor of noise in the measurements is the distribution of electron current from the electron gun. This gun current can be measured and corrected for. The current from the gun is measured in the illumination aperture before the electron beam hits the sample. The range of the current is approximately $2.4 \cdot 10^{-10}$ - $3.2 \cdot 10^{-10}$A.

First, it has to be determined what the relation is between the gun current and intensity measured in the detector without taking into account the reflectiveness of the sample. This can be calculated using mirror mode frames, in which all electrons are reflected before hitting the sample. Fig. 4.4 shows a strong linear fit between the current and measured intensity, using the maximum intensity of the diffraction spot as reference.

While the linear fit has an intercept, this has not been taken into account when correcting for gun current. Mathematically this should be included, as is shown in the derivation in appendix B, but there is also a figure included in the appendix showing the resulting IV curve when the intercept has also been corrected for. This could be due to the fact that intensity drops exponentially for $E > 0$. Hence, small noise factors in the fit, which have some impact on the intercept, will lead to an exponentially larger impact at higher energies. Also, it is possible that the intercept is not

exactly equal for every pixel on the linecut. If the 'base' intensity is lower, effectively, the linear fit will be moved down, changing the intercept. To take the intercept into account as well, one could determine a fit to the gun current in mirror mode for every distinct pixel and correct the individual pixels using these fits.

Rather, the relative gun current compared to the average gun current is used. At the frame with energy E, this correcting factor $B_{GCC,E}$ is calculated:

$$B_{GCC,E} = \frac{\frac{1}{N}\sum_{n=1}^{N} GC_n}{GC_E} \tag{4.7}$$

With GC_E the gun current at the frame with energy E. Hence, the resulting intensity for every pixel in that frame, will be:

$$I_{GCC,E} = B_{GCC,E} I_E \tag{4.8}$$

Fig. C.1 shows an IV curve of a sample with $NbSe_2$ flakes. Fig. C.1(c) has been corrected for gun current, as well as corrected for energy dispersion and averaged as described in 4.1.1 & 4.1.2 respectively. Visually, the curve has been improved, as it looks significantly smoother than the regular average.

Fig. C.1(b) and (d) again show the squared first differences as described in eq. (4.6). The gun current corrected squared first differences look smoother than the squared first differences of the regular average, especially for $E > 0$. The effect as in section 4.1.2 can be seen, with a smooth peaking value of the squared first difference approaching the first dip. This is again due to smoothing and an increase in the slope. This shows an increase in energy resolution. In appendix C, another gun current corrected IV curve is shown, with comparable characteristics in improvement.

4.2 In situ exfoliation

This section will focus on the exfoliation on TMDs. 'Normal' exfoliation is quite easy of regular substrates (Si/SiO_2 wafers), but rarely render large flakes of monolayers. Alternatively, exfoliation using substrates with a layer of gold will be discussed. Further, oxidation of flakes is problematic for some TMDs, as it might happen quickly and might change the

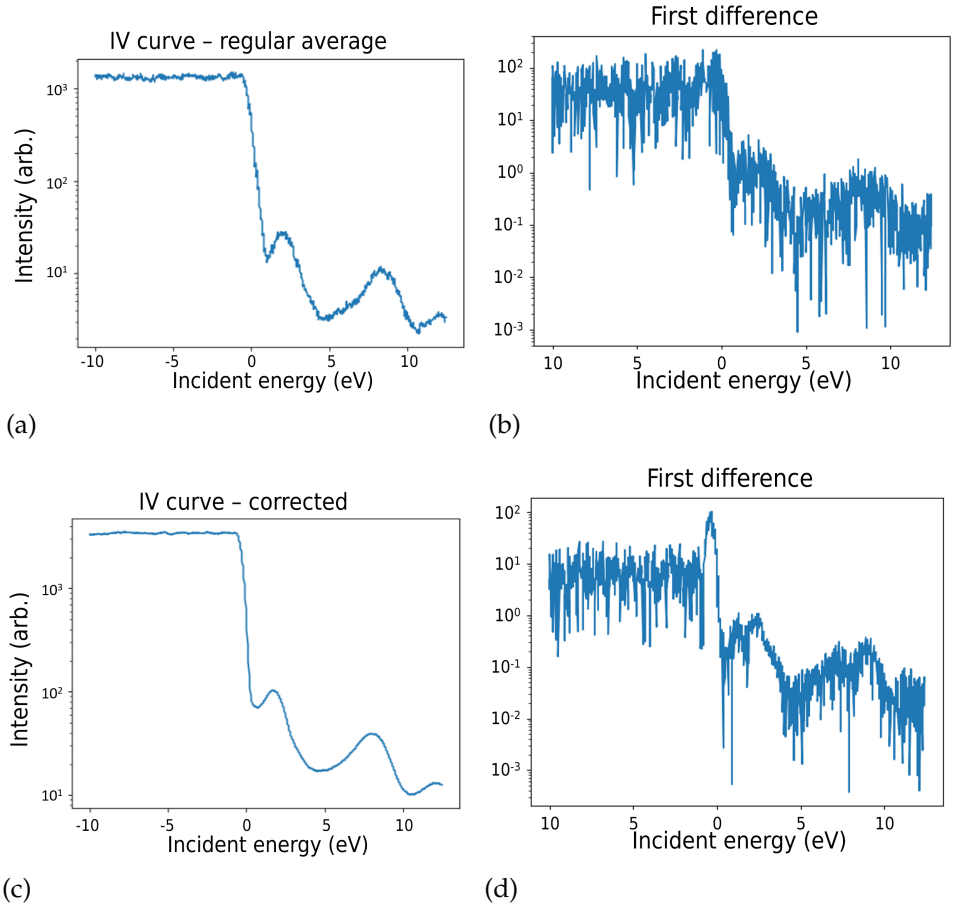

Figure 4.5: ***(a)*** *IV curve of $NbSe_2$, calculated with the regular average over a line-cut* ***(b)*** *First difference of IV curve shown in (a)* ***(c)*** *Improved IV curve, corrected for gun current, energy dispersion & and normalized before averaging* ***(d)*** *First difference of IV curve shown in (c). As was the case in fig. 4.3, the corrected IV curve is visually smoother. When taking the first difference of the uncorrected and corrected IV curve, (b) & (d), again, a smoother trend can be seen in the first differences of the corrected IV curve, while the first differences of the uncorrected IV curve is more erratic. Around $E = 0$, when transitioning from mirror mode to the first dip, a peaking curve can be seen in de corrected first differences, demonstrating a more smooth and pronounced slope in the corrected IV curve.*

properties, depending on the TMD. A method of in situ exfoliation, i.e. exfoliation in vacuum is also discussed in the section.

4.2.1 Exfoliation on substrate with Au

The most straight forward substrates for TMD exfoliation are Si or SiO_2 wafers. While this method works reasonably well, ending up with a noteworthy monolayer is rare. The contact between the substrate and the TMD does not provide enough interaction to cleave up to a monolayer, as the Van der Waals force between the substrate and bottom layer has to compete with the interlayer Van der Waals force [28]. An improved alternative is a substrate, e.g. Si/SiO_2, with a thin layer of gold evaporated, with a thickness of around 2-3 nm. Au atoms interact strongly with atoms of the chalcogen group. This group conveniently provides the atoms for TMDs that are closest to the substrate when exfoliating. Together with its low chemical reactivity and air stability, a substrate with a layer of Au is the perfect candidate to create monolayers of TMDs [29]. This method yields monolayers of typically several hundreds of microns [30].

Exfoliating on Si/SiO_2 substrates rendered little to no monolayers, whereas using a substrate with an Au layer did. The substrates have a basis of a regular wafer of Si or SiO_2. This wafer is chemically cleaned. Next and adhesive layer of 2 nm Cr is evaporated onto the wafer. Finally, a layer of either 2 or 3 nm is evaporated on the Cr layer. Fig. 4.6(a) shows a very thin MoS_2 flake of around 100 microns in width on a Si substrate evaporated with Au, with an adhesive layer of Cr between the wafer and Au. The thickness of flakes, i.e. the number of layers, can only be judged visually, as it is especially difficult to find thin flakes on Si substrates with gold under the optical microscope in the AFM. Visually however,we judge that these flakes are indeed thin. Fig. 4.6(b) shows another sample with a SiO_2 substrate with Au. A number of smaller thin flakes of around 50 microns are visible, with fig. 4.6(c) & (d) an AFM scan and linecut profile of the sample shown in (b) respectively. In the profile, a plateau can be observed with a thickness of 0.6-0.7 nm. This value corresponds very well to the values for monolayers found in other research [31].

4.2.2 Exfoliation in the LEEM loadlock vacuum

To prevent oxidation on TMD flakes, exfoliation should happen in an inert environment. The loadlock of the LEEM provides suitable conditions for

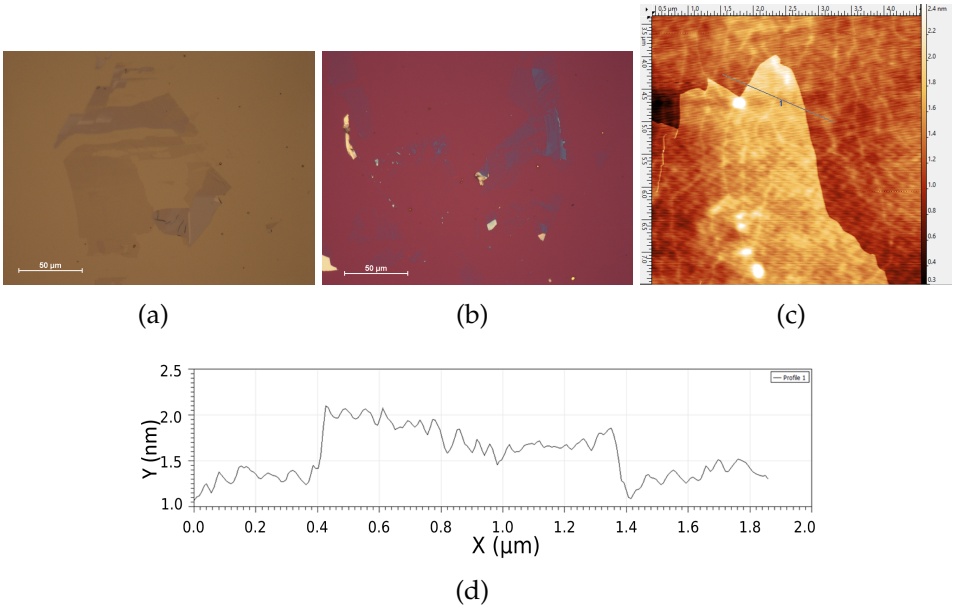

Figure 4.6: ***(a)*** *Thin-layer flake of MoS_2 on a Si substrate with a layer of Cr, and a layer of Au* ***(b)*** *Number of thin-layer flakes of MoS_2 on a SiO_2 substrate with a layer of Cr, and a layer of Au* ***(c)*** *AFM scan of sample shown in (b)* ***(d)*** *Profile of linecut in (c). Both samples show considerable few- or monolayer flakes of MoS_2, with the off-color patches thin flakes. The AFM scan of the SiO_2 sample shown in (c) & (d) finds a plateau with 0.6-0.7 nm thickness. This is in line with the literature value of MoS_2 monolayers [31].*

this. The lockload provides a vacuum of around 10^{-6} mbar. This low pressure and the fact that a sample typically does not remain in the loadlock longer than a couple of minutes, one can expect that freshly cleaved TMD flakes inside the loadlock are not significantly affected by oxidation. This might also be subject of further research.

In section 3.5, two different potential exfoliation techniques are described. Firstly, the method of full exfoliation manually ex situ. Then, a piece of Kapton tape is placed onto the substrate. This is placed in situ, inside the loadlock. When the vacuum is reached, the Kapton tape is removed, exfoliating the top layers from the settled flakes, revealing unaffected layers. Alternatively, the exfoliation process can happen ex situ, up to the action of putting the tape onto the substrate and exfoliating. Instead, flakes are collected by a piece of Kapton tape, which is placed on a clean substrate. Then, after putting the sample with the tape inside the loadlock and the desired vacuum is reached, the tape is removed, leaving unoxidized layers exposed on the substrate.

For both techniques, a screw is used to apply the Kapton on the exposed area of the sample in the sample holder. This screw with tape then has to be removed by moving the transfer arm. To do this in a controlled manner, a tool is designed which can be conveniently placed right below the access of the loadlock, fitting in a circular cavity on the floor of the loadlock. The semicircle is designed for the shaft of the screw to be able to get caught onto the tool. This tool is shown in fig. 4.7(a)-(c), and an example of a screw with Kapton tape is shown in fig. 4.7(d).

While both techniques of exfoliation in situ are possible, the technique with flakes deposited fully in situ is preferred. This is due to the fact that, while this technique might result in fewer flakes, one can assume that every resulting flake is freshly cleaved. This is in contrast to the other technique, where one cannot be directly certain whether a flake is freshly cleaved.

Because of the promising results of this technique, we will only focus on this method. Fig. 4.8(a)-(b) show a Si substrate sample with MoS_2 flakes deposited with this technique. While the screw accidentally separated from the sample before the loadlock was pumped into vacuum, under the optical microscope, we can visually assume these are MoS_2 flakes. There is a clear imprint of the screw head on the sample (fig. 4.8(a)). Zooming in, in fig. 4.8(b), there are plenty of flakes of reasonable size ($\tilde{1}$5 microns)

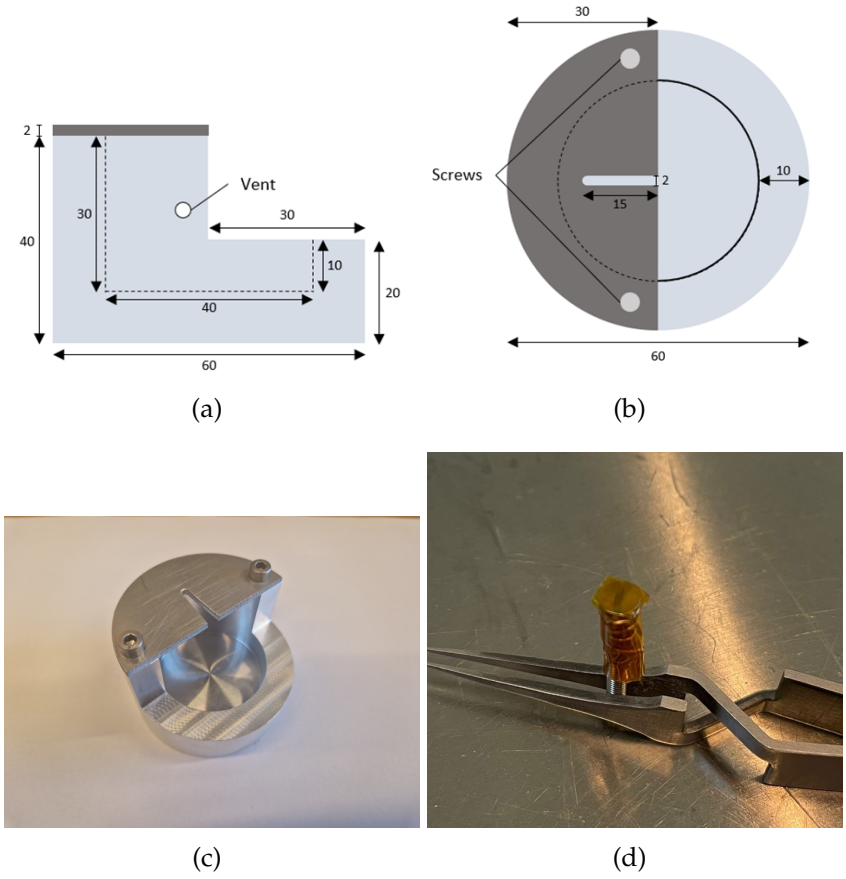

Figure 4.7: (a)-(b) *Design of exfoliation tool* ***(c)*** *Realized exfoliation tool* ***(d)*** *Screw with Kapton tape used for exfoliation. The tool shown in (a)-(c) can be placed inside the loadlock LEEM. The screw in (d) is adhered to the sample. By moving the transfer arm in the loadlock, the tool can catch onto the screw, pulling off the Kapton tape from the sample, intended to exfoliate TMD flakes on the substrate.*

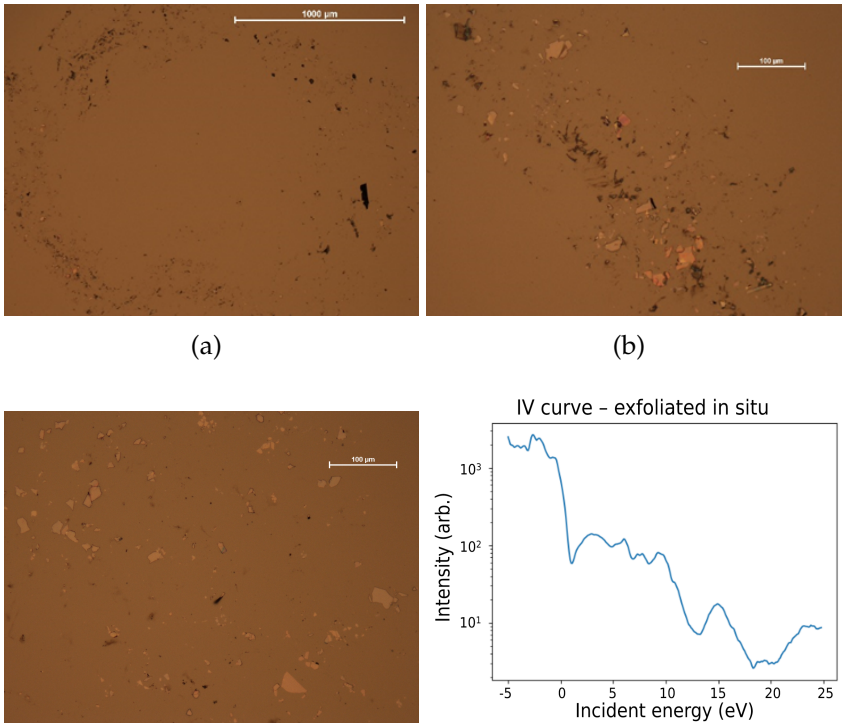

(a) (b)

(c) (d)

Figure 4.8: (a)-(b) *Sample of MoS_2 flakes on Si substrate. Deposited with screw onto the substrate (outside vacuum). There is a clear imprint of the screw head in (a). While no LEEM measurement has been done on this sample, it has been analyzed under the optical microscope, which confirms flakes on the substrate.* ***(c)*** *Sample of MoS_2 flakes on Si substrate after LEEM measurements. Deposited with screw inside the loadlock onto the substrate* ***(d)*** *IV curve of sample shown in (c). The roughness of the IV curve might be the result of some contamination.*

visible. The amount of flakes is evidence the technique works well. Fig. 4.8(c) shows a sample of Si substrate with MoS_2 flakes deposited with the same technique. This sample was measured in the LEEM, resulting in the IV curve shown in fig. 4.8(d). While the flakes are MoS_2, the irregular IV curve shows that the flakes are not very clean.

Chapter 5

Conclusion & Outlook

5.1 Conclusion

This thesis inspected a number of noise factors in LEEM measurements of transition metal dichalcogenides (TMDs). It discusses the source of these factors, and how to reduce this. One of the energy-resolution limiting aspects is the energy dispersion of electrons in LEEM. Electrons emitted from the electron gun, which hit the sample with a certain landing energy, have a specific distribution of kinetic energy due to tunnelling effects while being extracted from the electron gun. In diffraction space measurements, this influences the incidence and measuring angle of electrons. Up until now, this distribution has not been explicitly taken into account when analyzing LEEM data. Averaging ordinarily over pixels also averages this energy dispersion effect, limiting the resolution. The thesis proposed a method that not only corrects for not taking into account this effect but uses this effect to reduce overall noise. Further, although it has been possible to analyze the fluctuations in the number of emitted electrons from the gun, i.e. the gun current, it had not been used to reduce noise introduced by these fluctuations. Here, we show that explicitly measuring gun current can be used to improve measurements.

This research also explored methods of exfoliation. First, it analyzed an alternative exfoliation technique. Obtaining monolayers of TMDs on 'traditional' substrates proved to be difficult. Alternatively, exfoliating on a substrate evaporate with a thin layer of gold gave much more promising results, with few-layer flakes exfoliated of around 100 microns. Further, to prevent oxidation in TMD flakes, it set the basis for exfoliating in situ, specifically inside the loadlock of the LEEM, where the pressure gets

pumped down to around 10^{-6} mbar. While this is a good subject for further research, this thesis showed promising first results. This might be of use to further research into oxidation of TMDs.

5.2 Outlook

The results and conclusions of this thesis give multiple reasons for further research. One subject that needs more research is noise reduction in ARRES. The conclusions of energy dispersion focused on one certain position in diffraction space, that is the Γ spot. The methods might be extrapolated to ARRES measurements; it might be possible to use the energy dispersion for the diffraction spots at every position in diffraction space. That might require very accurately spaced steps in k-space, which would make it possible to link diffraction spots at different landing energy 'loops'. Further, the correction for gun current could also be further explored. The mathematically feasible correction of a linear fit of gun current to intensity did not provide improvements on measurements. As the data available for gun current is at the moment limited, more data might lead to new insights. Different kinds of fit could be investigated, as well as pixel-by-pixel correlation to the fit.

A lot of follow-up research can be done about in situ exfoliation. There is evidence that in situ exfoliation works, but exceptionally clean flakes have not been observed. Also, this might provide a basis for exfoliation in higher vacuums, up to ultra-high vacuum (UHV), which reaches pressures of at maximum 10^{-9}. This is possible in the sample chamber of the Leiden LEEM, but not in the loadlock. Moreover, while this research looked at exfoliation on gold, and in situ exfoliation separately, a subject of interest remains if exfoliation on gold works as well on in situ as ex situ. Due to the reactivity between Au atoms and chalcogen atoms, this might favour exfoliation with the tools proposed in the research. Also, the process of oxidation in TMDs might be of interest. Currently, there is no fast and distinct way to determine whether a TMD flake is oxidized in the LEEM. Additionally, successful in situ exfoliation might help research into the rate of oxidation of different TMDs. Unoxidized flakes could be exposed to controlled oxygen flow, to determine the effect on different chemically composed TMDs, or even if the number of layers has any influence on the oxidation process. The broad range of application options for the LEEM, as well as the range of properties of (oxidized) TMDs offer a great number of motivations for new research.

Version of July 5, 2023– Created July 5, 2023 - 14:16

Appendix A

Full width at half maximum for the electron gun

The energy per pixel is determined at $\delta = 2.275 \cdot 10^{-2} \pm 2.4 \cdot 10^{-6}$ eV. By measuring the number of pixels between the values at half maximum intensity for multiple mirror mode frames, the following full width at half maximum for the electron gun is calculated at: $FWHM = 0.24 \pm 0.01$ eV.

This is quite significant as LEEM measurements are typically done with an energy interval of 0.1 eV. This means there will be significant spillover in measuring points if the energy dispersion is not explicitly taken into account.

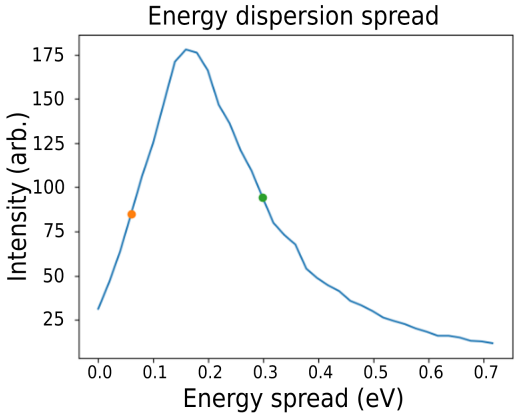

Figure A.1: *Full width at half maximum of the electron gun*

Appendix B

Gun current correction derivation with intercept

Multiple mirror mode measurements with gun current values seem to confirm the hypothesis that there is a linear relation between gun current and measured intensity. This is no surprise, as intensity measured is proportionate to the number of electrons, which is proportionate to the gun current. This would mean the relation looks as following:

$$I = \alpha + \beta GC \tag{B.1}$$

With I the intensity, α the intercept, and β the slope. To correct for gun current, the intensity at a certain point has to be corrected to some base intensity, for which can take the intensity corresponding to the mean gun current:

$$I_{mean} = \alpha + \beta GC_{mean} \tag{B.2}$$

Rearranging the terms and deviding the two equations for the data point and average:

$$\frac{I - \alpha}{I_{mean} - \alpha} = \frac{\beta GC}{\beta GC_{mean}} = \frac{GC}{GC_{mean}} \tag{B.3}$$

Rearrange the terms:

$$\frac{I - \alpha}{GC/GC_{mean}} = I_{mean} - \alpha \tag{B.4}$$

To obtain the base I_{mean}:

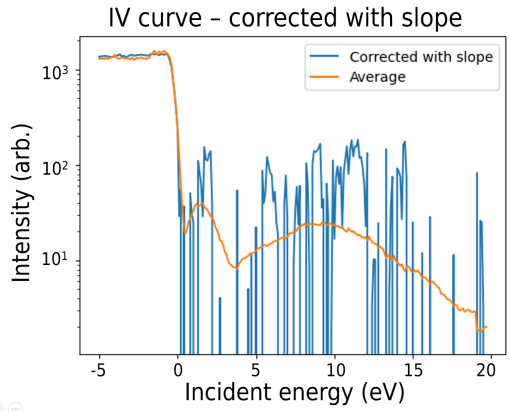

Figure B.1: *IV curve of regular average & IV curve corrected for gun current with intersect. For $E > 0$, noise factors seem to impact the correction yielding no improvement*

$$I_{mean} = \frac{I - \alpha}{GC/GC_{mean}} + \alpha \tag{B.5}$$

While this is mathematically correct, calculating these values and plotting these "corrected" values gives fig. B.1. This is obviously not an improvement of the IV curve. As mentioned in section 4.1.3, this might be due to the difference of true intersect for each individual pixel. Further, inaccuracies in fit might also play a role.

Appendix C

Additional gun corrected IV curve

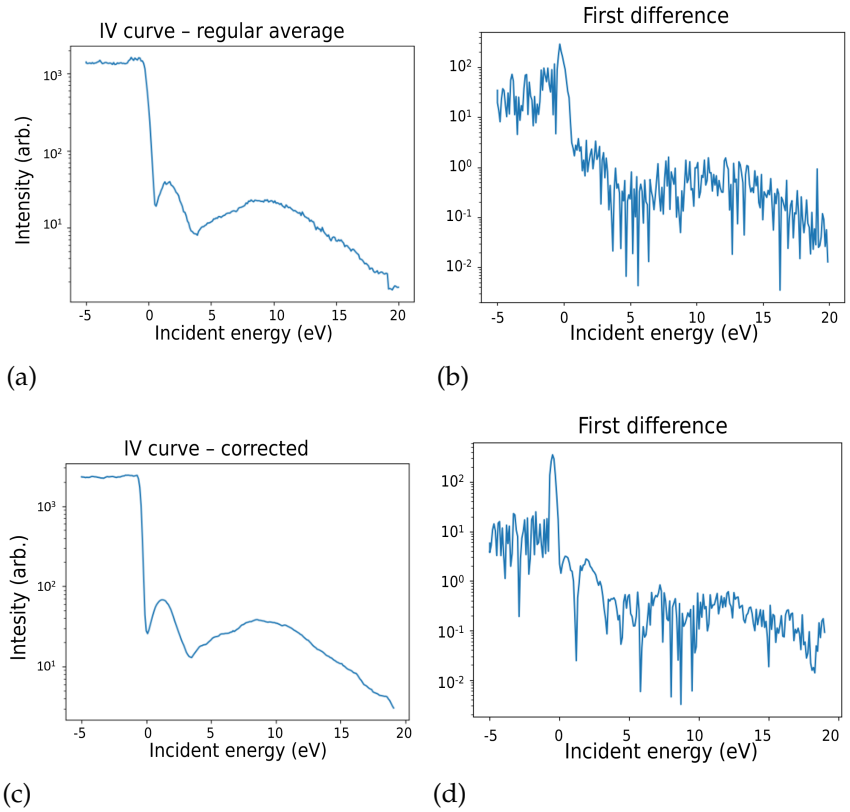

Figure C.1: ***(a)*** *IV curve of $NbSe_2$, calculated with the regular average over a line-cut* ***(b)*** *First difference of IV curve shown in (a)* ***(c)*** *Improved IV curve, corrected for energy dispersion & gun current, weighted average over pixels* ***(d)*** *First difference of IV curve shown in (c)*

Appendix D

Code

Energy dispersion correction & weighted average

```
#data: linecut
#egy: energy array
#reference_frames: frames to use as reference to stack
   lines on top of eachother

def averaging_trick(data,egy,reference_frames):
    no_frames = len(data.T)
    total_egy_delta = egy[-1] - egy[0]
    delta_per_frame = total_egy_delta/no_frames


    cut = len(data.T) - round((len(data) * epp)/
       delta_per_frame)
    full_corrected_linecut = np.empty((len(data), cut))


    for pixel in range(len(data)):
        corrected_linecut = []
        shift_left = pixel * epp
        cut_left = round(shift_left/delta_per_frame)
        shift_right = (len(data)-pixel) * epp
        cut_right = math.ceil(shift_right/
           delta_per_frame)
        if (cut_left+cut_right) < len(data.T)-len(
           full_corrected_linecut.T):
            cut_right += (cut_left+cut_right)-(len(data.
               T)-len(full_corrected_linecut.T))
```

```
        if (cut_left+cut_right) > len(data.T)-len(
            full_corrected_linecut.T):
            cut_right -= (cut_left+cut_right)-(len(data.
                T)-len(full_corrected_linecut.T))
        if cut_right == 0:
            full_corrected_linecut[pixel,:] = data[pixel
                ,cut_left:]
        else:
            full_corrected_linecut[pixel,:] = data[pixel
                ,cut_left:-cut_right]
    ratios = []
    ref_index = np.argmax(data[:,0])
    ref = full_corrected_linecut[ref_index,:
        reference_frames]
    for pixel in range(len(full_corrected_linecut)):
        ratio = [i / j for i, j in zip(
            full_corrected_linecut[pixel,:150], ref)]
        av_ratio = np.mean(ratio)
        ratios.append(av_ratio)

    corrected_for_ratios = np.empty_like(
        full_corrected_linecut)
    for pixel in range(len(full_corrected_linecut)):
        corrected_for_ratios[pixel,:] =
            full_corrected_linecut[pixel,:] / ratios[
            pixel]

    average_corr_data = np.mean(corrected_for_ratios,
        axis = 0)

    plt.semilogy(egy[:reference_frames],
        average_corr_data[:reference_frames])
    plt.title('IV curve averaged over corrected pixels')
    plt.ylabel('Intensity (arb.)')
    plt.xlabel('Incident energy (eV)')
    plt.show()
    return average_corr_data
```

Gun current correction

```
#This shift is necessary because there are sometimes
    shifted datapoints in gun current. Determines the
```

```
   shift based on best linear fit.
#linecut: napari linecut
#guncurrent: gun current array
#MMwindow: no. of frames in mirror mode
#shift: max guncurrent frameshift

def shiftdata_current(linecut,guncurrent,MMwindow,shift)
   :
    MM_guncurrent = guncurrent[:MMwindow]
    MM_intensity = np.mean(linecut[:,:MMwindow],axis=0)
    no_missingpoints = len(np.where(MM_guncurrent > 0))
       +1
    slicedcurrent = MM_guncurrent[no_missingpoints:]
    intercepts = []
    stderrors = []
    for i in range(-shift,shift):
        if i < 0:
            x = slicedcurrent[-i:]
            y = MM_intensity[:(i-no_missingpoints)]
        if i == 0:
            x = slicedcurrent
            y = MM_intensity[:-no_missingpoints]
        if i > 0:
            x = slicedcurrent[:-i]
            y = MM_intensity[i:-no_missingpoints]

        fit = stats.linregress(x,y)
        print(fit.stderr,fit.intercept)
        stderrors.append(fit.stderr)
        intercepts.append(fit.intercept)
    bestshift = range(-shift,shift)[np.argmin(stderrors)
       ]
    gc_intercept = intercepts[np.argmin(stderrors)]

    if bestshift < 0:
        corrected_gc = guncurrent[no_missingpoints-
           bestshift:]
        corrected_lc = linecut[:,:(bestshift-
           no_missingpoints)]
    elif bestshift == 0:
        corrected_gc = guncurrent[no_missingpoints:]
        corrected_lc = linecut[:,:-no_missingpoints]
    elif bestshift > 0:
```

```
        corrected_gc = guncurrent[no_missingpoints:-
            bestshift]
        corrected_lc = linecut[:,bestshift:-
            no_missingpoints]
    return corrected_gc, corrected_lc, gc_intercept

def guncurrent_correction(linecut,guncurrent,intercept):
    averageguncurrent = np.mean(abs(guncurrent))
    relative_gc = abs(guncurrent)/averageguncurrent
    corrected_I = ((linecut-intercept)/relative_gc)+
        intercept
    return corrected_I

#FWHM
def fwhm(spread,stepsize):
    maximum = max(spread)
    halfmax = maximum/2
    for i in range(len(spread)-1):
        if spread[i] <= halfmax and spread[i+1] >=
            halfmax:
            lower_index = i
        if spread[i] >= halfmax and spread[i+1] <=
            halfmax:
            upper_index = i
    EELS = np.arange(0,len(spread)*stepsize,stepsize)
    plt.plot(EELS, spread)
    plt.plot(lower_index*stepsize,spread[lower_index],'o
        ')
    plt.plot(upper_index*stepsize,spread[upper_index],'o
        ')
    plt.xlabel('EELS spread (eV)')
    plt.ylabel('Intensity (arb.)')
    plt.title('Full width at half maximum')
    plt.show()
    diff_index = upper_index - lower_index
    fw_hm = diff_index*stepsize
    print('Full width at half maximum:', fw_hm)
    return fw_hm
```

Bibliography

[1] Pulickel Ajayan, Philip Kim, and Kaustav Banerjee. Two-dimensional van der Waals materials. *Physics Today*, 69(9):38–44, 09 2016. ISSN 0031-9228. doi: 10.1063/PT.3.3297. URL https://doi.org/10.1063/PT.3.3297.

[2] Qing Hua Wang, Kourosh Kalantar-zadeh, Andras Kis, Jonathan Coleman, and Michael Strano. Electronics and optoelectronics of two-dimensional transition metal dichalcogenides. *Nature Nanotechnology*, 7:699–712, 11 2012. doi: 10.1038/nnano.2012.193.

[3] H. Hibino, H. Kageshima, F. Maeda, M. Nagase, Y. Kobayashi, and H. Yamaguchi. Microscopic thickness determination of thin graphite films formed on SiC from quantized oscillation in reflectivity of low-energy electrons. *Phys. Rev. B*, 77:075413, Feb 2008. doi: 10.1103/PhysRevB.77.075413. URL https://link.aps.org/doi/10.1103/PhysRevB.77.075413.

[4] Li F Mattheiss. Band structures of transition-metal-dichalcogenide layer compounds. *Physical Review B*, 8(8):3719, 1973.

[5] Andrea Splendiani, Liang Sun, Yuanbo Zhang, Tianshu Li, Jonghwan Kim, Chi-Yung Chim, Giulia Galli, and Feng Wang. Emerging photoluminescence in monolayer mos2. *Nano Letters*, 10(4):1271–1275, 2010. doi: 10.1021/nl903868w. PMID: 20229981.

[6] Peter S. Neu, Daniël Geelen, Aniket Thete, Rudolf M. Tromp, and Sense Jan van der Molen. Complementary LEEM and eV-TEM for imaging and spectroscopy. *Ultramicroscopy*, 222:113199, 2021. ISSN 0304-3991. doi: https://doi.org/10.1016/j.ultramic.2020.113199. URL https://www.sciencedirect.com/science/article/pii/S0304399120303399.

[7] Wonbong Choi, Nitin Choudhary, Gang Hee Han, Juhong Park, Deji Akinwande, and Young Hee Lee. Recent development of two-dimensional transition metal dichalcogenides and their applications. *Materials Today*, 20(3):116–130, 2017. ISSN 1369-7021. doi: https://doi.org/10.1016/j.mattod.2016.10.002. URL https://www.sciencedirect.com/science/article/pii/S1369702116302917.

[8] Phaedon Avouris, Tony F Heinz, and Tony Low. *2D Materials*. Cambridge University Press, 2017.

[9] Vera Janssen. *Electronic Properties of (Pseudo-) Two-Dimensional Materials*. PhD thesis, Delft University of Technology, 2020.

[10] Sefaattin Tongay, Hasan Sahin, Changhyun Ko, Alex Luce, Wen Fan, Kai Liu, Jian Zhou, Ying-Sheng Huang, Ching-Hwa Ho, Jinyuan Yan, et al. Monolayer behaviour in bulk ReS_2 due to electronic and vibrational decoupling. *Nature Communications*, 5(1):1–6, 2014.

[11] Rafael Roldán, Jose A. Silva-Guillén, M. Pilar López-Sancho, Francisco Guinea, Emmanuele Cappelluti, and Pablo Ordejón. Electronic properties of single-layer and multilayer transition metal dichalcogenides MX_2 (M = Mo, W and X = S, Se). *Annalen der Physik*, 526 (9-10):347–357, 2014.

[12] Xiaofeng Fan, David J. Singh, and Weitao Zheng. Valence band splitting on multilayer MoS_2: Mixing of spinâorbit coupling and interlayer coupling. *The Journal of Physical Chemistry Letters*, 7(12):2175–2181, 2016. doi: 10.1021/acs.jpclett.6b00693. PMID: 27225320.

[13] Peter S. Neu, Makars Šiškins, Eugene E. Krasovskii, Rudolf M. Tromp, and Sense Jan van der Molen. Electron transmission and mean free path in molybdenum disulfide at electron-volt energies. *Phys. Rev. B*, 107:075427, Feb 2023. doi: 10.1103/PhysRevB.107.075427. URL https://link.aps.org/doi/10.1103/PhysRevB.107.075427.

[14] Xisai Zhang, Yang Li, Wenqian Mu, Wenqi Bai, Xiaoxue Sun, Mingyu Zhao, Zhijie Zhang, Fukai Shan, and Zhenyu Yang. Advanced tape-exfoliated method for preparing large-area 2D monolayers: A review. *2D Materials*, 8(3):032002, may 2021. doi: 10.1088/2053-1583/ac016f. URL https://dx.doi.org/10.1088/2053-1583/ac016f.

[15] Hongsheng Liu, Nannan Han, and Jijun Zhao. Atomistic insight into the oxidation of monolayer transition metal dichalcogenides:

from structures to electronic properties. *RSC Adv.*, 5:17572–17581, 2015. doi: 10.1039/C4RA17320A. URL http://dx.doi.org/10.1039/C4RA17320A.

[16] Yun Kim, JinâLin Huang, and Charles M. Lieber. Characterization of nanometer scale wear and oxidation of transition metal dichalcogenide lubricants by atomic force microscopy. *Applied Physics Letters*, 59(26):3404–3406, 12 1991. ISSN 0003-6951. doi: 10.1063/1.105689. URL https://doi.org/10.1063/1.105689.

[17] Sebastian Markus Schramm. *Imaging with aberration-corrected low energy electron microscopy*. PhD thesis, Leiden University, 2013.

[18] TA de Jong. *Superlattices in van der Waals materials: a low-energy electron microscopy study*. PhD thesis, Leiden University, 2022.

[19] Johannes Jobst, Jaap Kautz, Daniël Geelen, Rudolf M Tromp, and Sense Jan Van Der Molen. Nanoscale measurements of unoccupied band dispersion in few-layer graphene. *Nature Communications*, 6(1): 8926, 2015.

[20] J. Jobst, E.E. Krasovskii, R. Ribeiro, T.A. de Jong, C.R. Dean, R.M. Tromp, and S.J. van der Molen. Evolution of unoccupied bands in the series of MoX_2 transition metal dichalcogenides (X = S, Se, Te) *(unpublished)*.

[21] Junqiang Xu Haiying Xu Dongqing Yang Xiaopeng Li Jikang Fan, Yong Peng and Qi Zhou. Numerical simulation of beam current control mechanism in the thermionic electron gun. *Vacuum*, 164:278–285, 2019. ISSN 0042-207X. doi: https://doi.org/10.1016/j.vacuum.2019.03.040. URL https://www.sciencedirect.com/science/article/pii/S0042207X1930048X.

[22] Ralph Howard Fowler and L. Nordheim. Electron emission in intense electric fields. *Proceedings of the Royal Society of London. Series A, Containing Papers of a Mathematical and Physical Character*, 119 (781):173–181, 1928. doi: 10.1098/rspa.1928.0091. URL https://royalsocietypublishing.org/doi/abs/10.1098/rspa.1928.0091.

[23] Arjo Andringa. A Novel Technique to Study Surface Profiles of Two-Dimensional Materials in LEEM. Master's thesis, Universiteit Leiden, the Netherlands, 2017.

[24] Yu-Chuan Lin, Riccardo Torsi, David B. Geohegan, Joshua A. Robinson, and Kai Xiao. Controllable thin-film approaches for doping and alloying transition metal dichalcogenides monolayers. *Advanced Science*, 8(9):2004249, 2021. doi: https://doi.org/10.1002/advs.202004249.

[25] Sergio Giacomo Sammartano. Outgassing rates of PEEK, Kapton® and Vespel® polymers. Master's thesis, Arcada, Helsinki, Finland, 2017.

[26] Stephen E. Swiontek and Akhlesh Lakhtakia. Vacuum-metal-deposition and columnar-thin-film techniques implemented in the same apparatus. *Materials Letters*, 142:291–293, 2015. ISSN 0167-577X. doi: https://doi.org/10.1016/j.matlet.2014.12.038. URL `https://www.sciencedirect.com/science/article/pii/S0167577X14022046`.

[27] Wolfram Jaegermann and Dieter Schmeisser. Reactivity of layer type transition metal chalcogenides towards oxidation. *Surface Science*, 165 (1):143–160, 1986.

[28] Max Heyl and Emil JW List-Kratochvil. Only gold can pull this off: mechanical exfoliations of transition metal dichalcogenides beyond scotch tape. *Applied Physics A*, 129(1):16, 2023.

[29] Yuan Huang, Yu-Hao Pan, Rong Yang, Li-Hong Bao, Lei Meng, Hai-Lan Luo, Yong-Qing Cai, Guo-Dong Liu, Wen-Juan Zhao, Zhang Zhou, et al. Universal mechanical exfoliation of large-area 2d crystals. *Nature Communications*, 11(1):2453, 2020.

[30] Gábor Zsolt Magda, János Pető, Gergely Dobrik, Chanyong Hwang, László P Biró, and Levente Tapasztó. Exfoliation of large-area transition metal chalcogenide single layers. *Scientific Reports*, 5(1):14714, 2015.

[31] Branimir Radisavljevic, Aleksandra Radenovic, Jacopo Brivio, Valentina Giacometti, and Andras Kis. Single-layer MoS_2 transistors. *Nature Nanotechnology*, 6(3):147–150, 2011.